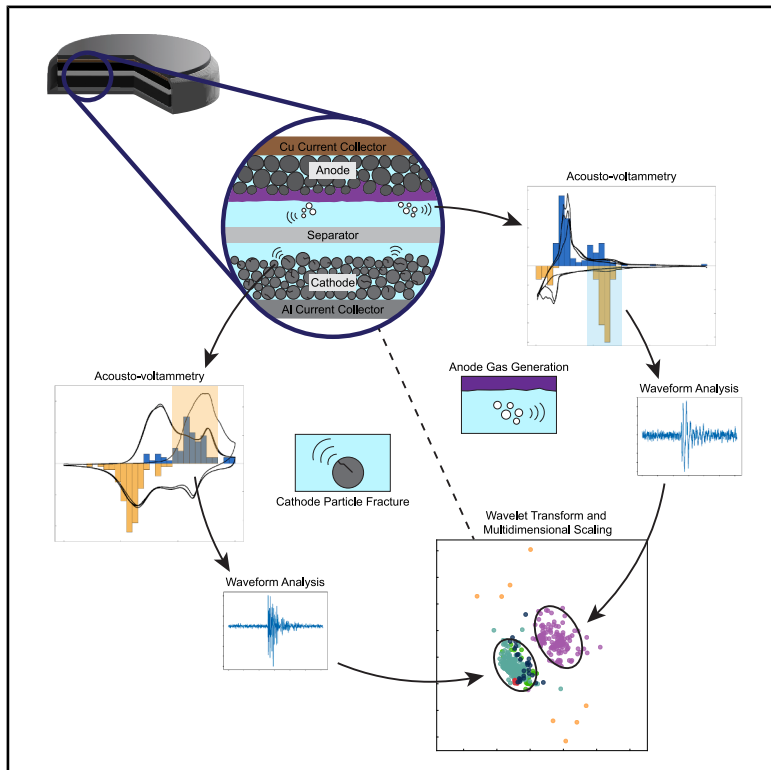


# Electrochemically resolved acoustic emissions from Li-ion batteries

## Graphical abstract



## Authors

Yash Samantaray, Daniel A. Cogswell,  
Alexander E. Cohen, Martin Z. Bazant

## Correspondence

bazant@mit.edu

## In brief

An *operando*, non-destructive evaluation method is proposed for Li-ion battery characterization, combining passive acoustic emissions analysis with simultaneous electrochemical testing. By filtering electromagnetic interference and applying wavelet transform-based signal processing, the approach reproducibly identifies and distinguishes internal physical mechanisms, such as gas generation and particle fracture.

## Highlights

- Acousto-voltammetry links acoustic signals to gas generation and particle fracture
- Reproducible acoustic emissions analysis requires filtering electromagnetic noise
- Wavelet-transformed acoustic emissions can distinguish distinct battery mechanisms
- Acoustic emissions analysis enables non-destructive battery degradation evaluation

Article

# Electrochemically resolved acoustic emissions from Li-ion batteries

Yash Samantaray,<sup>1</sup> Daniel A. Cogswell,<sup>1</sup> Alexander E. Cohen,<sup>1</sup> and Martin Z. Bazant<sup>1,2,3,\*</sup>

<sup>1</sup>Department of Chemical Engineering, Massachusetts Institute of Technology, Cambridge, MA 02139, USA

<sup>2</sup>Department of Mathematics, Massachusetts Institute of Technology, Cambridge, MA 02139, USA

<sup>3</sup>Lead contact

\*Correspondence: [bazant@mit.edu](mailto:bazant@mit.edu)

<https://doi.org/10.1016/j.joule.2025.102108>

**CONTEXT & SCALE** Over the lifetime of a Li-ion battery, various internal mechanisms, such as electrode material degradation and side reactions, can take place. The timing and location of these processes critically influence whether they enhance battery performance or shorten cycle life and increase safety risks. Conventional battery diagnostics primarily rely on voltage and current measurements and are often unable to detect internal mechanisms that do not directly influence macroscopic electrochemical variables. In this work, we present an *operando* non-destructive evaluation (NDE) method for Li-ion battery characterization that can provide insight into such internal mechanisms. This approach integrates acoustic emissions analysis, a well-established NDE technique in structural engineering, with controlled electrochemical testing. By implementing engineering controls to suppress electromagnetic interference, we achieve reproducible detection of internal events such as particle fracture and gas generation, as corroborated by scanning electron microscopy and gas detection methods, respectively. In addition, wavelet transform-based signal processing is used to distinguish acoustic waveforms associated with different underlying mechanisms. This proof-of-concept study establishes a methodology for characterizing physical internal mechanisms in electrochemical systems that cannot be adequately assessed through conventional health and safety metrics.

## SUMMARY

New methods of *operando* non-destructive evaluation (NDE) are needed to better assess the health and safety of Li-ion batteries. Acoustic emission (AE) testing is a widely used NDE technique in structural engineering but has yet to provide reliable assessments in battery applications. Here, we show that various electro-chemo-mechanical processes in battery electrodes (graphite and nickel-manganese-cobalt oxides [NMC]) can be reproducibly identified by electrochemically resolved AEs after eliminating electromagnetic interference and applying wavelet-based signal processing. First, we perform “acousto-voltammetry” to correlate acoustic activity with specific electrochemical processes, such as ethylene gas generation and NMC particle fracture, as confirmed by gas detection and *ex situ* scanning electron microscopy (SEM) imaging, respectively. Next, we demonstrate that AEs can be distinguished using wavelet-transform features. Electrochemically resolved AEs provide a new window into quantitatively monitoring battery degradation, offering insights into electro-chemo-mechanical processes and potential advantages over conventional methods for the assessing state of health, remaining useful life, and safety risks.

## INTRODUCTION

Li-ion batteries (LIBs) are ubiquitous energy storage devices for consumer electronics and electric vehicles due to their high energy density, low self-discharge, and long lifetime.<sup>1</sup> However, a number of complex degradation mechanisms are known to occur in LIBs to varying degrees based on electrode material, electrolyte, cycling protocol, and environmental factors.<sup>2,3</sup> These processes are difficult to quantify during operation and

challenging to use for predicting battery lifetime and safety. As a result, new methods to estimate the state of health (SoH) or state of safety (SoS) of LIBs and monitor the (micro)structural condition of the internal components must be developed to engineer safer, longer-lasting batteries.<sup>4</sup>

Many non-destructive evaluation (NDE) methods exist for LIBs, including electrochemical,<sup>5–7</sup> thermal,<sup>8</sup> and imaging techniques.<sup>9,10</sup> Each method has advantages and disadvantages in terms of cost, accuracy, time required, sensitivity, and ability

to be performed during *operando* conditions.<sup>11</sup> Acoustic emission (AE) testing is a popular NDE technique used throughout various fields of engineering and, to a limited extent, for electrochemical devices to study material fracture, deformation, corrosion, deposition, and gas evolution by analyzing the number and energy of AE signals.<sup>12–14</sup> AE testing has similarities with ultrasonic techniques (UTs) through the shared use of acoustic activity; however, AE testing is a purely passive method of detecting small releases of energy due to physical processes in the form of an acoustic (pressure) wave in a system, while UT requires the active input of an acoustic signal and measures the change in bulk modulus and density of a system through the reflection or transmission of the signal.<sup>15–18</sup>

Recently, AE analysis has been used for evaluating LIB health and estimating remaining useful life.<sup>19–23</sup> However, despite the demonstrated potential of AE analysis for LIBs, little interpretation of the acoustic data is typically provided, likely due to the lack of reproducibility in battery-AE data and the limited number of publications that report data from more than one battery-AE experiment. A brief overview of the existing literature of AE testing of batteries and battery materials is provided in the supplemental information (Section S1),<sup>19,21,24–36</sup> and a thorough description of the technique and analysis of past battery-AE studies was provided in a recent review.<sup>37</sup>

In addition to reproducibility, another challenge is correlating AEs to specific processes that occur in LIBs. Previous battery-AE studies analyzed AE features such as peak or average frequency, partial power intervals, rise time, duration, and acoustic energy.<sup>38–40</sup> While informative, these variables neglect important multiresolution features of AEs, and previous studies that used these variables often struggled to distinctly correlate groups of AEs to specific processes or to classify all AEs.<sup>30,32,41–43</sup> Electrode events, such as Li (de)intercalation, solid electrolyte interphase (SEI) formation, Li plating, and particle fracture, often occur in overlapping potential and time windows during conventional constant current cycling.<sup>44,45</sup> By contrast, cyclic voltammetry (CV), in which a cyclic sweeping modulation of potential is applied to an electrode and the resulting current measured, can more easily distinguish between internal processes that occur at different potentials.<sup>46</sup> Such “polarographic methods” have become powerful tools of electroanalytical chemistry, as recognized by the first Nobel Prize in the field of electrochemistry awarded to Heyrovsky in 1959.<sup>47</sup>

Here, we describe a hybrid technique termed “acousto-voltammetry,” in which battery-AE testing is performed simultaneously with CV to electrochemically resolve AEs from specific battery mechanisms. Two case studies using graphite and nickel-manganese-cobalt oxide (NMC) electrodes in Li-ion half-cell batteries are presented, along with methods to improve reproducibility in battery-AE experiments. Quantitative particle fracture analysis by scanning electron microscopy (SEM), comparison to gas evolution data from literature, and control experiments with Li-symmetric cells are used to corroborate battery mechanism identification. Finally, we show that unsupervised clustering techniques using features drawn from the wavelet transform (WT) allow for interpretability and distinguishability between AE waveforms generated by graphite electrodes, NMC electrodes, and noise.

## RESULTS AND DISCUSSION

### Improved reproducibility of AE experiments through noise removal

Initial acousto-voltammetry experiments on graphite and NMC half-cells produced cumulative AEs per cell that varied by an order of magnitude (Figure 1C). The reproducibility of the cumulative number of AEs across identically constructed and cycled Li-ion cells was significantly improved (Figure 1D; Section S2.1) with the addition of electromagnetic interference (EMI) chokes (Figures 1A and 1B). Conventional EMI is undesired noise in an electrical path that takes the form of a high-frequency signal (generally in the high MHz to GHz range, but can be present at kHz as well) that can occur when current flows through unshielded wires near a system of interest.<sup>48</sup> EMI chokes, such as ferrite beads, function by acting as low-pass filters and present a high impedance to high-frequency signals and a low impedance to lower-frequency signals.<sup>48</sup> While previous battery-AE work took great care to prevent vibrational interference through experimental isolation, AE voltage (decibel [dB]) thresholding, and background noise testing, EMI noise reduction was limited to removing AEs with short duration or low voltage threshold crossing count. We later demonstrate that EMI noise emissions can take several forms that are not always caught by a post-processing low-count filter, and thus believe EMI noise contributed significantly to the large variation in cumulative AEs both across studies using the same electrode material and within individual experiments.

### Acousto-voltammetry on polycrystalline NMC811 half-cells

NMC811 half-cells ( $\text{Li} \parallel \text{NMC811}$ ) were tested by acousto-voltammetry across a potential range wider than conventionally experienced during constant current cycling. The use of CV as the simultaneous electrochemical measurement during AE testing allowed for precise time and potential resolution of the phase transformations that occur in NMC cathodes. The electrochemically resolved AEs across four consecutive cyclic voltammograms on the same NMC811 half-cell (Figure 2A) showed two histogram peaks of acoustic activity, with one during delithiation (4.0–4.3 V) of the NMC811 electrode and another during lithiation (3.4–3.8 V). In literature, the  $\text{H}_2 \rightarrow \text{H}_3$  phase transition in NMC811 has been shown to occur over the same delithiation potential window. This phase transition has also been linked to particle fracture due to its rapid volume contraction.<sup>49,50</sup> Specifically in NMC811, the  $\text{H}_2 \rightarrow \text{H}_3$  phase transition represents the greatest c-axis change and rate of change across any reasonable lithiation state (Figure 2B).<sup>49</sup>

Dividing the electrochemically resolved AE analysis by cycle (Figures 2C–2F), the delithiation AEs predominantly occurred during the first two cycles. Most of the emissions in the first cycle occurred during the single current peak, which corresponds to an overlap of all three expected phase transitions ( $\text{H}_1 \rightarrow \text{M}$ ,  $\text{M} \rightarrow \text{H}_2$ , and  $\text{H}_2 \rightarrow \text{H}_3$ ). However, the specific phase transitions that occur during the highest rate of AEs can be narrowed down further. Through hybrid CV–incremental capacity testing (Figure S12), it can be determined that the  $\text{M} \rightarrow \text{H}_2$  and  $\text{H}_2 \rightarrow \text{H}_3$  phase transitions overlap with the potentials that are most

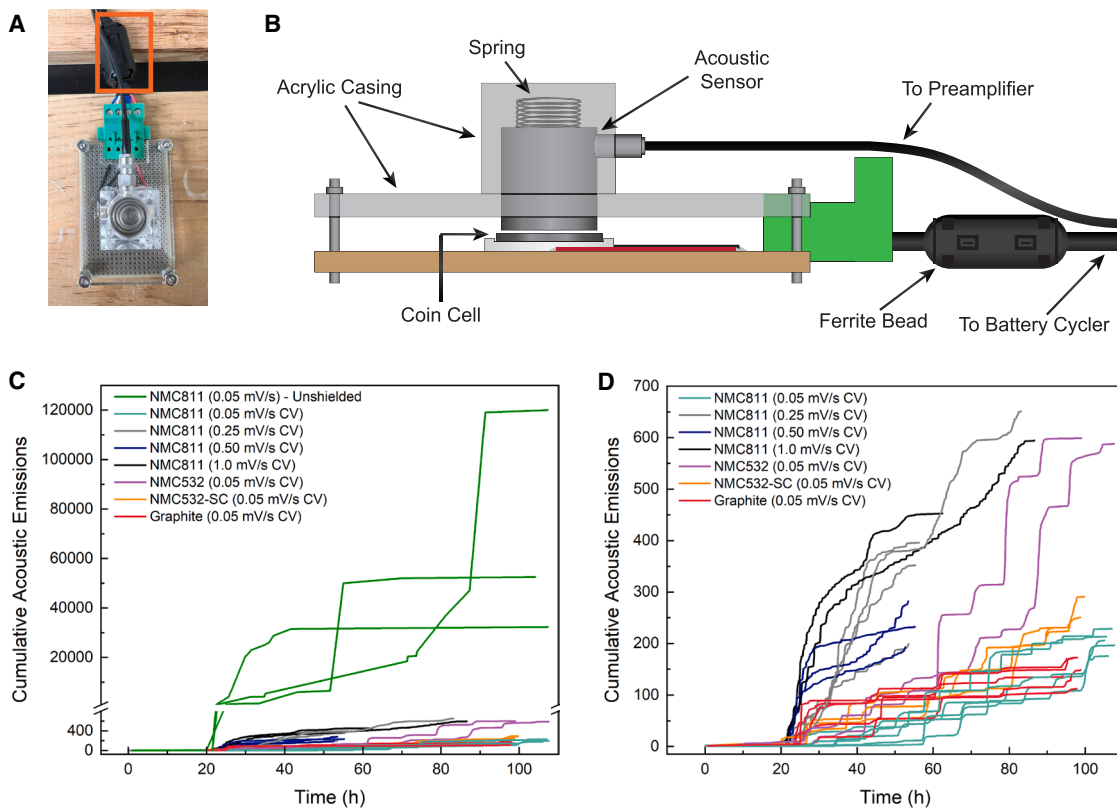


**Figure 1. Improved reproducibility of AE experiments through noise removal**

(A and B) Custom configuration for performing acousto-voltammetry experiments with coin cell batteries in (A) top view and (B) labeled side view schematic. A ferrite bead used as an EMI choke is highlighted by an orange box in part A. (C) Cumulative number of AEs detected during acousto-voltammetry experiments of NMC and graphite half-cells at different scan rates. Here, acoustic emissions refer to any instance in which the vibration measured by the acoustic sensor crosses the user-defined decibel (dB) threshold. Once a threshold crossing is detected, subsequent AEs were not counted within a 200  $\mu$ s window to avoid double-counting closely spaced events. The green traces, obtained from NMC811 half-cells without EMI chokes or filters on AE duration or counts, exhibited 2–3 orders of magnitude more AEs than the experiments with EMI chokes and filters. (D) Cumulative number of AEs detected during acousto-voltammetry experiments conducted with EMI chokes and filters. Traces of the same color represent experiments with the same material and CV scan rate. Acousto-voltammetry experiments at different scan rates demonstrate improved reproducibility. Additional statistical analyses on the reproducibility are detailed in [Section S2.1](#). More details on the effect of scan rate on the acousto-voltammetry experiments are shown in [Sections S1.5](#) and [S10](#).

acoustically active (4.05–4.25 V). The potentials at which the phase transitions occur in the subsequent cycles can be more clearly identified by the half-wave potential ( $E_{1/2}$ ) of each (de)lithiation current wave. The  $E_{1/2}$ s of the H1  $\rightarrow$  M, M  $\rightarrow$  H2, and H2  $\rightarrow$  H3 phase transitions for the NMC811 electrodes in this work are 3.75 V, 4.00 V, and 4.19 V, respectively, which are within 3 mV of the phase transition potentials of NMC811 determined by incremental capacity analysis on the same batch of electrodes ([Figures S13](#) and [S14](#)) and in literature.<sup>49</sup> The emissions in the second cycle occur near the current peaks from the M  $\rightarrow$  H2 and H2  $\rightarrow$  H3 phase transitions, corroborating the first cycle analysis.<sup>51</sup> In additional NMC811 half-cells tested by acousto-voltammetry ([Figures S5](#) and [S6](#)), the distributions of delithiation AEs were similar, with the two highest concentrations of acoustic activity during delithiation occurring at 4.1 V (dominated by first cycle AEs) and 4.15 V, respectively (generally between the M  $\rightarrow$  H2 and H2  $\rightarrow$  H3 phase transitions), demonstrating reproducibility.

A destructive assessment of NMC811 half-cells cycled to different potentials within the first cyclic voltammogram was conducted to assess the micro-structural changes throughout the potential range. The SEM imaging-based particle fracture ratio ([Figure 3A](#)) and particle fracture rate ([Figure 3B](#)) were calculated at each potential. The particle fracture ratio and rate increased near the delithiation H2  $\rightarrow$  H3 phase transition and decreased near the lithiation M  $\rightarrow$  H1 phase transition (the absolute value of the particle fracture rate is shown in [Figure 3B](#)). The change in particle fracture ratio can be qualitatively seen in the SEM images ([Figures 3C–E](#)). More details on the data collection and calculation are included in [Section S4](#).

In contrast to delithiation emissions, which occurred predominantly over the first two cycles and decreased over time, fewer lithiation AEs occurred during the first cycle but appeared in similar numbers during the later three cycles. A majority of the lithiation AEs occurred in the potential range during and directly after the M  $\rightarrow$  H1 transition. No significant morphological changes or side

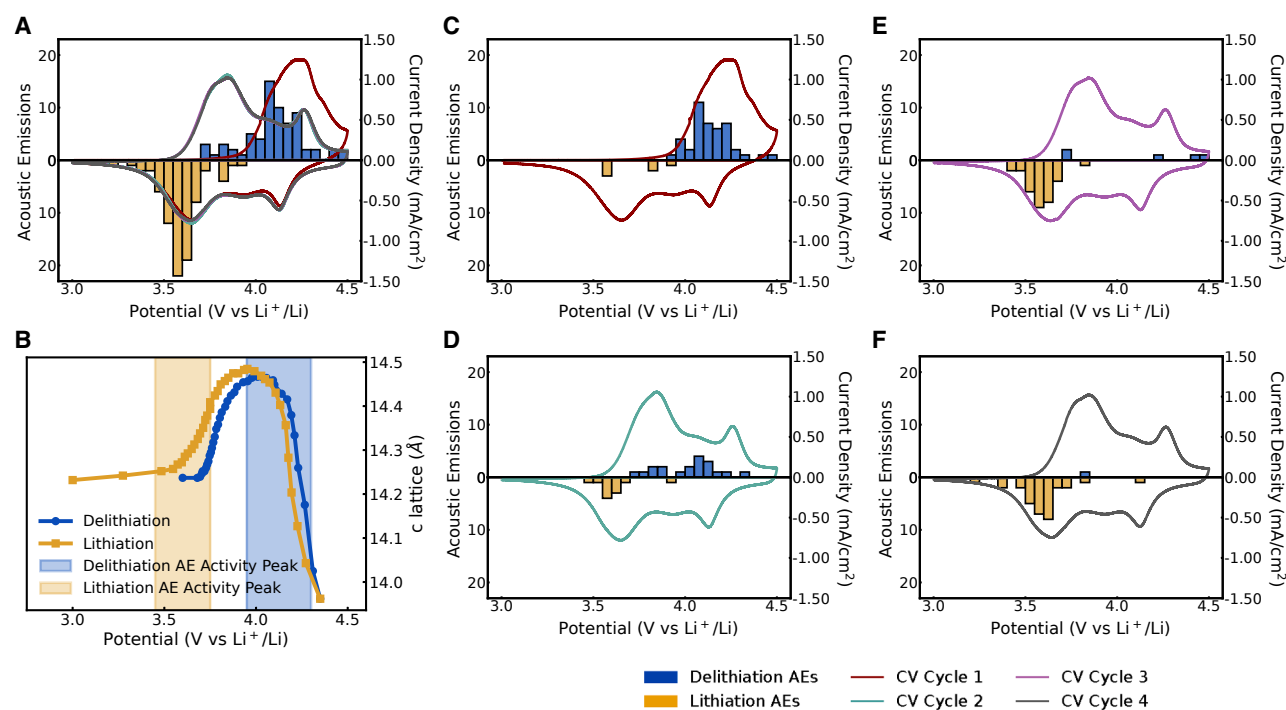


**Figure 2. Acousto-voltammetry on a polycrystalline NMC811 half-cell**

(A) Electrochemically resolved AEs during 4 consecutive cyclic voltammograms conducted at a scan rate of 0.05 mV/s between 3.0 and 4.5 V. The blue histogram indicates the total number of AEs detected at each potential during delithiation of the NMC811 cathode during the four cycles. The yellow histogram shows the total number of AEs detected at each potential during lithiation of NMC811 during the four cycles. The cyclic voltammograms are shown by the colored traces. (B) Operando XRD analysis of NMC811 half-cell during a C/10 constant current charge and discharge showing that the potential regions of greatest acoustic activity during delithiation (blue shading) and lithiation (yellow shading) occur during c-lattice contraction of the material (adapted from Li et al.<sup>49</sup>). (C–F) Electrochemically resolved AEs of the NMC811 half-cell in part A in the (C) 1<sup>st</sup>, (D) 2<sup>nd</sup>, (E) 3<sup>rd</sup>, and (F) 4<sup>th</sup> cycles.

reactions are expected at that potential; however, as confirmed by the SEM imaging data in this work and X-ray computed tomography data in literature,<sup>52,53</sup> a portion of the NMC fractures visually appears to close at this potential, as supported by X-ray diffraction (XRD) data indicating lattice contraction as well (Figure 2B).<sup>49</sup> The number and energy of AEs in this potential range are consistent in the third and fourth CV cycles, leading to the hypothesis that these emissions are caused by repeated chemo-mechanical deformation of the porous electrode during cycles of lithiation-induced swelling and shrinking. Under small deformations, the electrode composite behaves as an elastic body, but whenever a yield criterion is exceeded, irreversible plastic deformation and damage will occur. In powder composites such as these porous electrodes, the dominant plasticity mechanisms include frictional sliding of grain contacts above a critical shear stress<sup>54</sup> and consolidation or densification of the grain packing above a critical pressure.<sup>55</sup> In the mechanical model of electrode composites introduced by Zhu et al.,<sup>56</sup> these mechanisms are captured by Drucker-Prager<sup>57</sup> and Deshpande-Fleck<sup>58</sup> plasticity models, respectively, augmented by a hardening law<sup>56</sup> and the Anand-Gu flow rule.<sup>59</sup> Recently, Ipers et al.<sup>55</sup> incorporated Zhu's model in deformable porous electrode theory (DPET), which successfully predicted elasto-plastic deformation and irreversible swelling of battery electrodes during electrochemical cycling. We conjecture that the irreversible sliding and consolidation predicted by DPET simulations may cause the parti-

cle fractures associated with high-frequency AEs. However, it is beyond the scope of this paper to formulate or validate models incorporating physics-based simulations of AEs, which is left for future work.

#### Effects of particle agglomeration structure on the AEs of NMC532

To validate that the AEs being recorded were directly related to particle fracture, a crystallinity study using NMC532 as the active material was conducted. Single-crystal NMC materials have fewer crystal grain boundaries and are known to fracture less than polycrystalline samples.<sup>60,61</sup> Single-crystal NMC532 (NMC532-SC) and polycrystalline NMC532 (NMC532-PC) electrodes of similar areal capacity loading were assembled and tested using acousto-voltammetry.

Electrochemically resolved AE analysis of NMC532-PC half-cells revealed a different pattern in comparison to that of NMC811 (Figures 4A and S8). The lithiation AEs peaked across a similar potential range to the NMC811 half-cells (3.4–3.8 V), which correlates with the M → H1 phase transition in NMC532. However, the delithiation AEs peaked at a lower potential range (3.8–4.1 V), which correlates with the H1 → M phase transition in NMC532 (Figure 4A). This difference could be explained by the rapid volume change that occurs in this potential window for NMC532.<sup>62</sup> Unlike NMC811, NMC532 undergoes its greatest volume change during

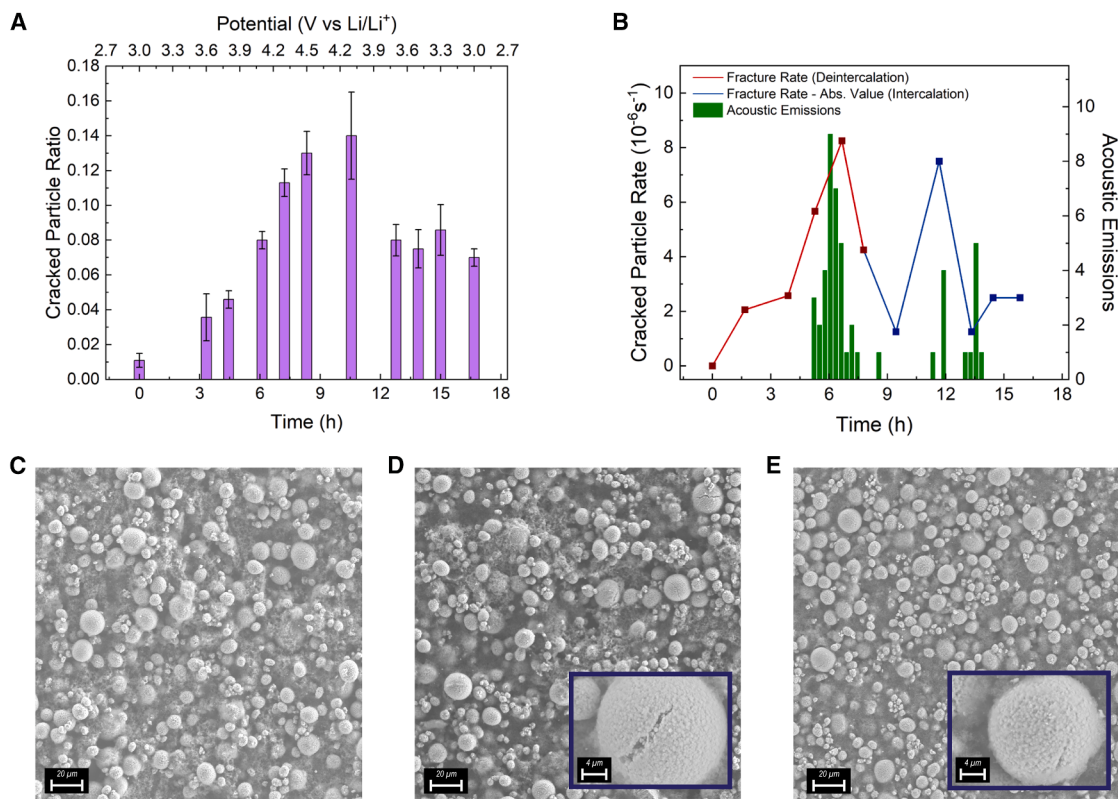


**Figure 3. Fracture analysis of NMC811 particles during acousto-voltammetry**

Particle fracture rate is correlated with periods of high acoustic activity, as validated by *ex situ* SEM analysis.

(A) Ratio of surface-fractured NMC811 particles to total number of NMC811 particles counted over at least three images for each of 2–3 cells at each potential shown across the first CV. Only particles above 10 μm in their largest dimension were considered for the analysis. Error bars represent the standard deviation across samples at each potential.

(B) Rate of NMC811 particle cracking calculated using the cracked particle ratio and the scan rate. Each value represents the linear interpolation of the rate as the midpoint between potentials with cracked particle ratios. The red curve represents the cracked particle rate during delithiation of NMC811. The blue curve represents the absolute value of the cracked particle rate during lithiation. The green bars are a histogram of the first cycle AEs during an acousto-voltammogram of NMC811.

(C) SEM image of an NMC811 electrode cycled to 3.6 V.

(D) SEM image of an NMC811 electrode cycled to 4.5 V. (D-insert) SEM image of a cracked individual particle from an NMC811 electrode cycled to 4.5 V.

(E) SEM image of an NMC811 electrode cycled up to 4.5 V and back to 3.0 V. (E-insert) SEM image of a cracked individual particle from an NMC811 electrode cycled to 4.5 V and back to 3.0 V.

the H1 → M phase transition potential window, which aligns well with the witnessed acoustic activity. The electrochemically resolved AE analysis of NMC532-SC half-cells displayed a similarly shaped distribution of AEs relative to the phase transformation potentials determined by the current peaks as in the NMC532-PC half-cells (Figures 4B and S9); however, there were significantly fewer AEs than in the NMC532-PC samples (<25%). The significant reduction of acoustic hits and energy in the NMC532-SC half-cells indicates that the majority of the acoustic activity detected in the NMC532-PC electrodes is due to particle fracture. As further confirmation, *ex situ* SEM imaging of NMC532-PC and NMC532-SC electrodes at high potential (4.6 V) revealed surface particle fracture in the NMC532-PC electrodes but significantly less in the NMC532-SC electrodes (Figures 4C and 4D; Section S5.1).

All three NMC materials displayed significant acoustic activity during the delithiation first cycle, but fewer emissions on subsequent cycles. These AEs may be correlated with particle fracture, as data in literature suggest that NMC particle fracture is expected to predominantly occur during the first few cycles and less so during further cycles.<sup>63</sup> This is also consistent with a battery-AE study conducted on LiNiO<sub>2</sub> (an end member of the ternary phase diagram of NMC cathodes).<sup>32</sup>

**Acousto-voltammetry on graphite half-cells**

Graphite half-cells were tested by acousto-voltammetry to investigate the AEs during SEI formation. The electrochemically resolved AEs across three consecutive cyclic voltammograms on the same graphite half-cell (Figure 5A) showed three peaks of acoustic activity: one during discharging or delithiation of the graphite electrode (positive current) between 0.2 and 0.5 V and two during charging of the graphite electrode (negative current), with one in the lithiation potential range (0.01–0.25 V) and the other at a higher potential (0.4–0.8 V). Each of the AE peaks

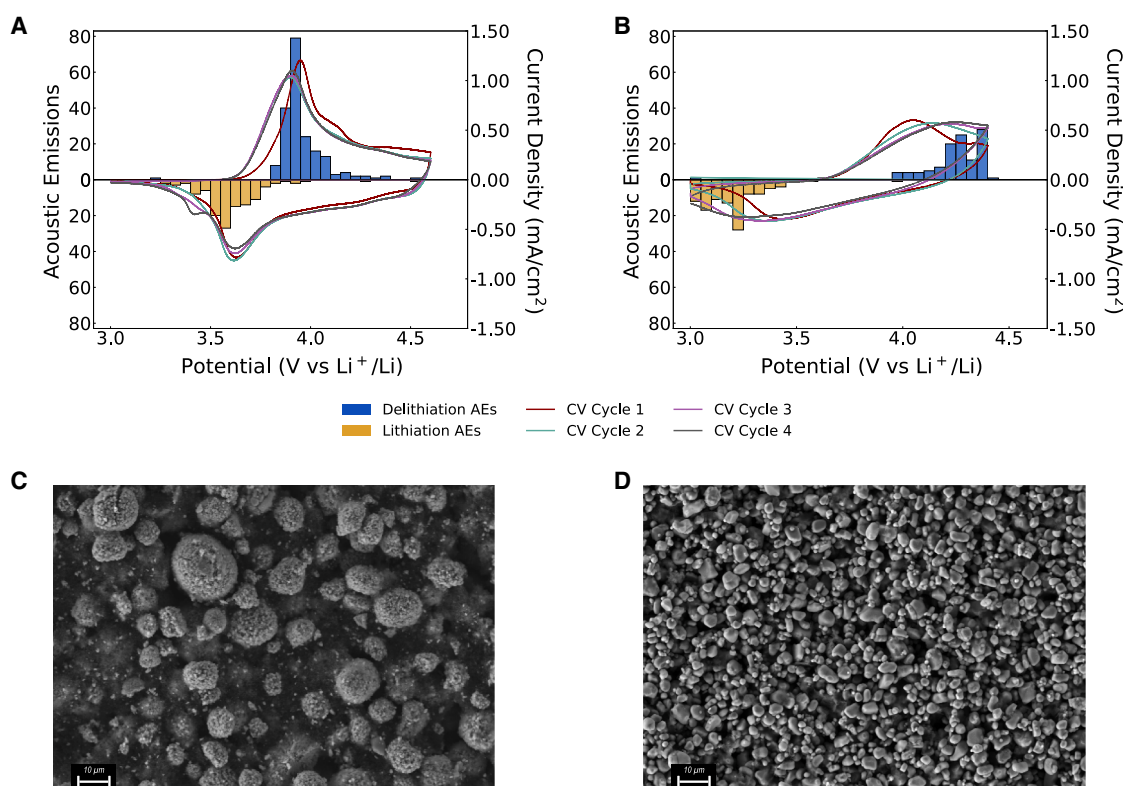


**Figure 4. Effects of particle agglomeration structure on the AEs of NMC532**

Single-crystal NMC532 displays significantly less acoustic activity and surface particle fracture.

(A) Electrochemically resolved AEs of a polycrystalline NMC532 (NMC532-PC) half-cell, including all AE signals detected during 4 CVs.

(B) Electrochemically resolved AEs of a single-crystal NMC532 (NMC532-SC) half-cell, including all AE signals detected during 4 CVs.

(C) SEM image of a cycled NMC532-PC electrode showing significant surface particle fracture.

(D) SEM image of a cycled NMC532-SC electrode showing limited surface particle fracture. Additional characterization of NMC532-PC and NMC532-SC electrodes is shown in [Section S5.1](#).

appears to overlap with current peaks in the cyclic voltammograms. The AE peak during graphite discharge overlapped with the delithiation current peak of the cyclic voltammogram, the low-potential AE peak during graphite charging overlapped with the lithiation current peak, and the high-potential AE peak during graphite charging overlapped with the irreversible current peak that occurred during the first cyclic voltammogram. The latter can be viewed clearly when the electrochemically resolved AE analysis is examined individually by cycle. [Figure 5B](#) directly shows the overlap between the AEs and the current peak generally associated with SEI formation. [Figures 5C and 5D](#) show the second and third cycle cyclic voltammograms without the clear SEI current peak and the corresponding AEs. The later cycles continued to have AEs during the lithiation and delithiation current peaks, but the number was significantly reduced as compared with the first cycle. The reproducibility of the electrochemically resolved AEs of the graphite half-cells can be seen in [Figures S10 and S11](#).

Similar to NMC cathodes, the AEs detected during (de)lithiation may result from particle fracture or exfoliation, which are known degradation mechanisms of graphite<sup>3,65</sup>; however, experimental validation of fracture in the graphite electrode was difficult to verify due to the lack of a common graphite

particle morphology in the pristine state ([Figure 5E](#)) and the growth of SEI, which impacts the surface view of the material ([Section S5.2](#)). Compared with the AEs during the (de)lithiation potential ranges, the AEs during the SEI formation potential range had longer durations and lower peak frequencies ([Table S3](#)). While past battery-AE studies have struggled to confidently match gas evolution with AEs, our results indicated that the potential range at which the acoustic activity occurred precisely overlaps with ethylene gas evolution measured in a similar experimental system using online electrochemical mass spectrometry ([Figure 5F](#)).<sup>64</sup> This result contrasts with the conclusion drawn from a battery-AE study conducted on a Super C65 (carbon black) and polymer binder electrode, in which chronoamperometry and CV were used simultaneously with AE analysis.<sup>31</sup> The authors claimed that gas evolution had no noticeable effect on the acoustic activity; however, roughly one-third of the AEs detected occurred during the first lithiation of the carbon and overlapped with a current peak around 0.4–0.8 V, indicative of SEI side reactions.<sup>31</sup> A similar peak in acoustic activity and current during this potential range was observed during acousto-voltammetry on carbon black electrodes conducted in this work ([Figures S26 and S27](#)).

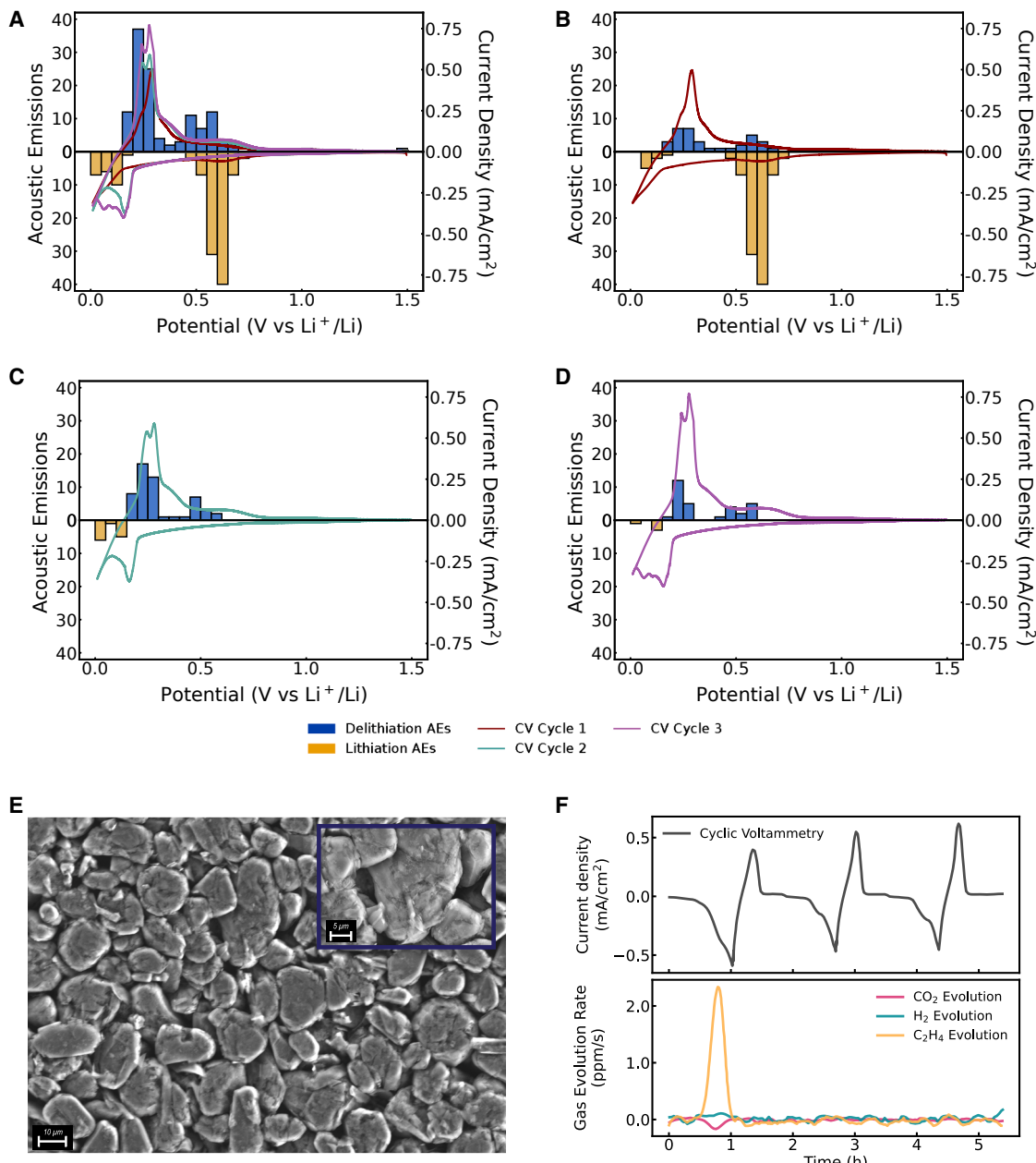


**Figure 5. Acousto-voltammetry on a graphite half-cell**

(A) Electrochemically resolved AEs during 3 consecutive cyclic voltammograms conducted at a scan rate of 0.05 mV/s between 0.01 and 1.5 V.

(B–D) The data in part A during the (B) 1<sup>st</sup>, (C) 2<sup>nd</sup>, and (D) 3<sup>rd</sup> cycles.

(E) SEM image of a pristine graphite electrode. (E-insert) SEM image of a pristine single graphite particle.

(F) Online electrochemical mass spectrometry data of gas evolution rate during graphite formation by CV, showing a peak in ethylene gas evolution rate during the potential range of SEI formation in the first cyclic voltammogram in a graphite half-cell (adapted from Zhang et al.<sup>64</sup>).

#### Battery-acoustic emissions testing system validation

To verify that the AEs detected during the acousto-voltammetry experiments represented processes occurring in the graphite or NMC electrodes, other spurious sources within the coin cell that could lead to additional acoustic hits and attenuation of the acoustic signal were also investigated.

Within the half-cell construction, the most likely source of AEs other than the cathode would be at the Li anode, which undergoes Li plating and stripping and SEI formation and cracking during the cyclic voltammogram. Previous studies have claimed that AEs of the Li anode can be neglected in half-cell experiments.<sup>27,32,41</sup> To verify this claim, AE testing of Li-symmetric

cells was conducted using CV over an extensive range of  $\pm 250$  mV, resulting in a maximum current density magnitude of approximately  $2.5 \text{ mA/cm}^2$ . Only 1–2 AEs per cycle were detected when the Li electrode was subjected to a current density less than  $1.5 \text{ mA/cm}^2$ ; however, approximately 3–4 AEs were detected per cyclic voltammogram above these two limits (Figures S28 and S29). From literature and Li-symmetric cell testing in this work, the overpotential experienced by the Li anode was positively and approximately linearly correlated with current density.<sup>27</sup> The potential regions of greatest acoustic activity in the NMC811 half-cells occurred when the current density was in the range of  $0.25$ – $1.25 \text{ mA/cm}^2$  and in the graphite half-cells when the current density was in the range of  $0.10$ – $0.75 \text{ mA/cm}^2$ . Therefore, while a few AEs could be from the Li anode, there should not be a substantial contribution, given the acoustic activity during the Li-symmetric tests.

Further confirmation that spurious AEs from the Li anode do not significantly impact the electrochemically resolved acoustic analysis came from investigating attenuation through the separator and electrolyte using inverted Li || NMC811 half-cells. The inverted half-cells were built by switching the locations of the electrodes during coin cell construction. The acoustic sensor remained in contact with the larger coin cell cap and thus in closer contact with the Li metal electrode. This setup had a similar distribution of electrochemically resolved AEs compared with the conventional Li || NMC811 half-cells, though with fewer total emissions (Figures S30 and S31). This reduction indicated the presence of attenuation when measuring AEs that cross through cell components, such as the separator and electrolyte. Lower energy emissions, such as those present during the M → H1 phase transition in NMC811 lithiation, may not be registered after crossing through the cell under the chosen sensitivity settings in this study.

Next, the potential for other components of the coin cell, such as the spring, to produce spurious AEs was investigated. AE testing of lithium iron phosphate (LFP) half-cells was conducted using the same coin cell components. LFP undergoes a similar unit cell volume expansion (6%–7%)<sup>66</sup> to NMC811 (5%–6%)<sup>67</sup> during (de)lithiation, resulting in a similar deformation of the spring within the coin cell while cycling. Virtually no AEs were detected during three cyclic voltammograms across the full (de)lithiation range (2.5 V–4.1 V) for the LFP half-cells (Figures S32 and S33), indicating that the coin cell structural components should have minimal impact on the detected AEs during the acousto-voltammetry experiments. Additionally, this result further corroborates the ability of the separator and electrolyte to attenuate the AEs from the Li anode, as an insignificant number of AEs were detected in the LFP half-cell experiments over a similar potential and current density range as in the NMC811 half-cell experiments.

Overall, variation in the number of emissions in the data reported in this work still remains but is most likely attributable to natural structural differences between individual electrodes. This is further supported by the SEM imaging data, in which minor differences in the particle fracture ratio or rate between cells cycled to the same potential are positively correlated with the minor differences in cumulative AEs and energy (Figures S17 and S18). In particular, this result underscores the sensitivity and accuracy of the acoustic emissions measurement.

### Distinguishability of battery AEs through WT and unsupervised clustering

AEs from graphite, NMC, and Li metal electrodes were identified and isolated from conventional EMI noise with validation through destructive assessment and careful experimental control. To further analyze these signals, we explored unsupervised clustering based on transformations of the pre-distinguished transient waveforms.

WTs were taken of AEs from several acousto-voltammetry experiments across different electrode materials in addition to WTs of AEs caused by EMI. AEs caused by physically tapping the bench near the experimental configuration were also added and denoted as “noise – vibration.” WT scalogram heatmaps of representative single emissions from each of the six groups (Figures 6A–6E and 6G) show differences in time-resolved frequency content. These differences can be analyzed using multi-dimensional scaling (MDS), an algorithm that attempts to preserve relative pairwise distances between WT scalograms (Figure S39) during dimensionality reduction. Initially, there were two distinct clusters of AEs: one composed almost entirely of AEs in graphite half-cell experiments during SEI formation and another consisting of NMC811 AEs (most likely from particle fracture and recombination), graphite (de)lithiation AEs, Li AEs, and a localized group of EMI noise AEs. The AEs caused by vibrational noise spanned a wide space around the two clusters (Figure S40). After applying AE filters based on duration and counts, a significant reduction in the number of noise emissions (EMI and vibration) can be seen while maintaining the identity and separation between the original two clusters (Figure 6). Further examples of acoustic waveforms, WTed-AEs, and summary acoustic features from each of the six groups are shown in Section S11.

The WT also enables comparisons to previous battery-AE studies that predominantly looked at peak frequency or duration as key AE features. Qualitative comparisons between the WTs of representative emissions from the six categories show that each group is visually distinct. EMI tends to be a wideband signal that stretches beyond 1 MHz with extremely short duration (Figure 6A). While many past battery-AE studies would have successfully eliminated many of these emissions by rejecting AEs with less than 2 counts, at least two other scalogram forms of EMI were discovered in our dataset. One includes the presence of multiple EMI emissions in a single transient AE, which incorrectly gives the appearance of a multiple count wave (Figure S37), and the other is a single-frequency, constant amplitude, long-duration EMI (Figure S38) emission, which has generally not been considered in previous studies, though manual removal was mentioned in a single battery-AE paper.<sup>28</sup> The vibration AEs (Figure 6B) have a low and narrowband frequency and a long duration, often greater than the 300  $\mu\text{s}$  window used for the analysis.

Graphite AEs during the lithium (de)intercalation potential ranges (Figure 6D) have a wideband frequency response with a relatively short duration (10–20  $\mu\text{s}$ ). By contrast, graphite AEs in the SEI formation potential range (Figure 6E) are generally narrowband signals with low frequency (70–100 kHz) and longer duration (25–45  $\mu\text{s}$ ) but are distinct from vibrational noise and long-duration EMI emissions by having a non-constant

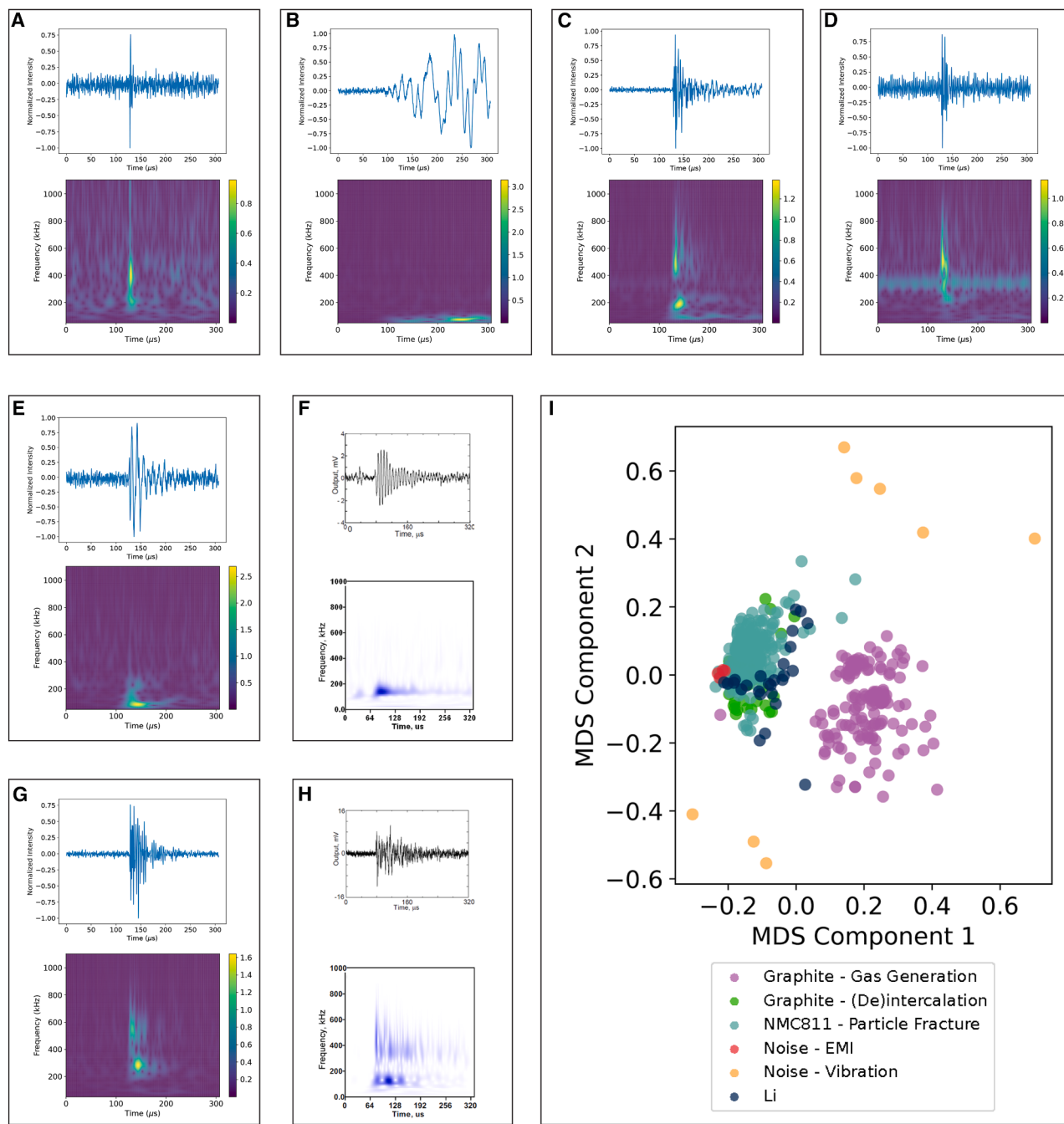


**Figure 6. Distinguishability of battery AEs through the WT and unsupervised clustering**

(A–H) Raw AE waves and corresponding WT scalograms of AEs (A) caused by EMI, (B) caused by vibrations generated by tapping the table near the experimental configuration, (C) from a Li-symmetric cell, (D) from graphite (de)intercalation (E) during the 1<sup>st</sup> cycle of a graphite half-cell in the SEI formation potential window, (F) during gas evolution induced on highly oriented pyrolytic graphite (reproduced from Matsuo et al.<sup>68</sup>), (G) from an NMC811 half-cell, and (H) during induced fracture of highly oriented pyrolytic graphite (reproduced from Matsuo et al.<sup>68</sup>).

(I) MDS plot of the WT AEs emissions from different acousto-voltammetry experiments and noise sources. The noise emissions were captured without EMI chokes or batteries present.

amplitude. Previous battery-AE studies believed these characteristics describe gas evolution emissions, and perhaps the most convincing data to support this hypothesis is from a

publication that also took the WT of an AE caused by electrochemically induced gas evolution on a graphitic electrode (Figure 6F).<sup>68</sup> Our study corroborates this for gas evolution

caused by SEI formation in an *operando* Li-ion cell, especially because other mechanisms, such as lithium (de)intercalation and particle fracture, are not expected to occur significantly in the potential range, given the slow-rate cyclic voltammogram and the staging nature of lithium intercalation into graphite.<sup>44,69</sup>

The NMC811 AEs (Figure 6G) have a wideband frequency response with a short duration (10–25 µs) similar to the graphite AEs during (de)intercalation. Because of these features, the NMC811 emissions tend to cluster near the traditional EMI noise emissions but generally have a significantly longer duration and higher count values. Previous battery-AE literature has suggested that particle fracture emissions tend to have a peak frequency above 500 kHz, which was seen in several WT scalograms of NMC811 AEs in this study. However, many AEs also take the forms seen in Figures S35 and S36, where the peak frequency varies within the wideband (distribution seen in Figure S41). Because these AEs still have a short duration and NMC811 only evolves significant amounts of gas above 4.4 V,<sup>70,71</sup> it does not appear that these emissions correspond to gas evolution. Further corroboration is found in the previous WT-AE study, in which AEs from induced fracture of a graphitic electrode appeared to have a similar wideband signal with a peak frequency around 160 kHz (Figure 6H).<sup>68</sup> The NMC811 result in particular highlights the utility of using the combination of acousto-voltammetry and the WT for AE hit classification.

Li AEs (Figure 6C) have similar duration (15–25 µs) and frequency data to NMC811 and graphite (de)intercalation emissions, which could potentially be explained by the continual stripping and refilling of the SEI shells on the Li anode surface. However, the distinction between the two lies in the amplitude of the AEs, in which the Li emissions are generally lower in energy (median energy of 0.42 aJ for Li AEs compared with 0.80 aJ for NMC811 AEs). More details comparing the signal features of all the AE categories can be found in Table S3.

A few NMC811 and Li AEs appear close to the graphite-SEI cluster. Interestingly, over 95% of the NMC811 AEs in the graphite-SEI cluster occur at a potential greater than 4.4 V (across several acousto-voltammetry experiments), which may indicate gas evolution from the cathode material. Similarly, for the graphite (de)lithiation AEs in the NMC811 cluster, over 90% of them occur during delithiation or below a potential of 0.3 V during lithiation. These AEs may be due to graphite particle fracture or delamination.

After applying the count and duration filters, we more effectively resolve the two clusters of AEs on the two-dimensional MDS plot, which potentially represent specific mechanisms, namely, gas generation emissions and particle fracture emissions (Figure 6I). It is important to note that some EMI and vibrational noise AEs still persist, despite the filters. Particularly concerning are EMI AEs, as they overlap with some NMC811 and Li AEs, indicating that certain particle fracture-type emissions have a similar time and frequency content to EMI emissions. The WT-MDS method could be utilized to remove any AEs that are close to the localized EMI noise AE group in the MDS plot. This process would potentially remove some real electrode-based AEs but would increase confidence in eliminating effects of EMI in the experiment. Ultimately, this result underscores that more complex waveform analysis methods beyond simple filters are

required to completely isolate EMI noise in battery-AE experiments.

## Conclusions

The methodology for performing electrochemically resolved acoustic emissions analysis using acousto-voltammetry was demonstrated on Li-ion half-cells to evaluate particle fracture in NMC811 and SEI formation on graphite *in operando*. After carefully eliminating acoustic noise due to EMI using engineering controls and battery-AE system validation, AEs were reproducibly detected when measured simultaneously with CV. Through comparisons with previous gas evolution experiments<sup>64</sup> and *ex situ* SEM analysis, correlations were corroborated between AEs and specific battery mechanisms, namely gas generation and particle fracture on graphite and NMC811 electrodes, respectively. Finally, signal processing using the WT enabled distinguishability between AEs arising from different proposed mechanisms and demonstrated that EMI and vibrational noise require more complex methods than count and duration filters to isolate. These results illustrate the capability of *operando* AE analysis as a sensitive and accessible NDE method for LIBs and potentially other electrochemical systems when performed in an electrochemically and temporally resolved manner.

## METHODS

### Cell fabrication

Hohsen CR2032 coin cells were used for all experiments (Al-CVD SUS 316L case, SUS 316L wave spring – 15 mm diameter by 1.4 mm height, SUS 316L spacer – 15.5 mm diameter by 0.5 mm thick). Cells were assembled in an Ar-filled glovebox ( $\text{H}_2\text{O} < 0.1 \text{ ppm}$ ,  $\text{O}_2 < 1 \text{ ppm}$ ). NMC811 (Nanomyte® BE-56E, NEI Corp, 2.0 mAh/cm<sup>2</sup> areal capacity), NMC532 (Nanomyte® BE-52E, NEI Corp, 2.0 mAh/cm<sup>2</sup> areal capacity), NMC532 single-crystal (LiFun Technology Co., 2.4–2.5 mAh/cm<sup>2</sup> areal capacity), LFP (Nanomyte® BE-60E, NEI Corp, 1.25 mAh/cm<sup>2</sup> areal capacity), and graphite (Nanomyte® BE-200E, NEI Corp, 2.4 mAh/cm<sup>2</sup> areal capacity) electrodes were cut into a circular shape with a 15.9 mm diameter and paired with a 15.6 mm diameter Li foil disk (0.45 mm thickness, Guangdong Canrd New Energy Technology Co.; estimated capacity >150 mAh). Additional details on the preparation of carbon black electrodes are included in Section S1.2. The positive and negative electrodes were separated by two 19 mm diameter Celgard 2325 separators. A total of 51 µL of electrolyte (1 M LiPF<sub>6</sub> in 1:1 EC:EMC, Sigma Aldrich) was added to each cell in 3 separate 17 µL aliquots, between the separators and between each separator and its adjacent electrode.

### Electrochemical characterization

The potential window for electrochemical testing was chosen based on the stability window of each material. The potential window was between 3.0 V and 4.5 V for Li || NMC811 half-cells, between 3.0 V and 4.6 V for Li || NMC532 (polycrystalline) half-cells, between 3.0 V and 4.4 V for Li || NMC532 single-crystal half-cells, between 2.5 V and 4.1 V for Li || LFP half-cells, and between 0.01 and 1.5 V for Li || graphite half-cells (all potentials are vs. Li<sup>+</sup>/Li).

All electrochemical testing was conducted using a multi-channel battery cycler (LBT20084, Arbin) at room temperature (22°C–24°C). NMC half-cells were tap charged to 3.0 V within 1 h of construction and held at that potential for 20 h to ensure complete wetting. LFP half-cells were tap charged to 2.5 V, graphite half-cells were tap charged to 1.5 V, and both were held for the same period of time. CV was performed at varied scan rates in the range of 0.05 to 1 mV/s across the specified voltage range. Each cell was cycled for at least 3 cyclic voltammograms.

### Acoustic emissions experimental configuration

During electrochemical testing, each cell was monitored using a single-ended wideband frequency acoustic emissions sensor (WS $\alpha$  100–1,000 kHz AE Sensor, Physical Acoustics Corp.). A custom coin cell holder was designed to keep the AE sensor in continuous direct contact with the positive electrode case of the coin cell (Figures 1A and 1B). This was accomplished by designing and machining an acrylic housing to contain the AE sensor and a spring. The housing allowed for repeatable alignment, x-y immobilization of the AE sensor, and a downward pressure to ensure continuous direct contact with the coin cell. An acoustic couplant gel (Echo 8 ZH™, Echo Ultrasonics) was placed on the surface of the coin cell prior to sensor placement to prevent air gaps between the case and the AE sensor. The coin cell was held in place under the AE sensor using a battery holder (1057TR, Keystone Electronics), which was connected to an Arbin LBT20084 channel, allowing for simultaneous electrochemical and acoustic emissions testing.

The AE sensor was connected to an in-line 2/4/6 preamplifier (2/4/6—Switch Selectable Gain Single-Ended and Differential Preamplifier, Mistras Group, Inc.) that was used with a single-ended configuration and a gain of 60 dB. The preamplifier had a built-in bandpass filter that restricted the observed frequency from 10 to 900 kHz. The data acquisition system (EXPRESS-8 – PCI Express-based Eight-channel AE Board & System, Physical Acoustics Corp.) was connected to the output of the preamplifiers. The AEwin for Express-8 software (Physical Acoustics Corp.) was used for acquisition, recording, and initial processing of the data. AEs detected with a duration less than 3  $\mu$ s or greater than 250  $\mu$ s and AEs with less than 2 counts were removed from the analysis. Hits measured on multiple channels within the same 10 ms window were removed as well.

An acoustic noise survey of the room was initially performed with the sensors resting on empty coin cell casings. A threshold value of 26 dB was sufficient to eliminate nearly all acoustic activity over the course of days, including events such as the opening and closing of nearby doors and foot traffic near the experiment. To demonstrate reproducibility, at least 3 cells with the same electrode material, coin cell construction (metallic components, separator, and electrolyte), and cycling condition (electrochemical procedure, scan rate, and voltage range) were tested for each result at separate times, with much of the data included in the Sections S2, S6, S7, S8, and S9.

In order to remove the influence of EMI on the battery-AE measurements, EMI chokes, such as ferrite beads and toroids, were added to all exposed current-carrying elements within 2 m of the

experiment. This included all power supply cables, electrical wires between the battery cycler and the experimental configuration, and connections between the AE sensor, preamplifier, and the acoustic hardware. Furthermore, a Faraday cage was constructed around the battery cycler. Prior to adding the EMI chokes and Faraday cage, AEs detected by the experimental configuration caused by turning the lights on and off (without a battery present) were recorded.

### Acoustic waveform analysis

A WT was conducted on each AE waveform in order to resolve its temporal structure in terms of frequency and duration.<sup>72,73</sup> A time window of 200  $\mu$ s was used for each waveform and adjusted so that the first threshold crossing of the wave occurred at 28  $\mu$ s. The algorithm was formulated using a complex Morlet wavelet with center and bandwidth frequencies of 1.5 and 1.0 respectively, as used in mechanical fault diagnosis.<sup>74</sup> The transform was conducted over the frequency range of roughly 50 kHz to 2.1 MHz. A distance matrix composed of pairwise root-mean-square distances between each transformed waveform was calculated. MDS,<sup>75</sup> an unsupervised learning algorithm for dimensionality reduction, was used to visualize the similarity and clustering of different waveforms in 2 dimensions. The use of other wavelet basis functions and parameters was explored further in Section S12.4.

### SEM characterization

SEM was performed with a Zeiss Merlin high-resolution SEM. Images were taken with an accelerating voltage of 15 kV and a current of 7–10 nA. Samples were prepared in an Ar glovebox and kept in an airtight container under Ar until loading onto the SEM stage (<1 min exposure to air).

### NMC811 particle fracture analysis

Li || NMC811 half-cells were cycled at 0.05 mV/s to different potentials within the first cyclic voltammogram before disassembling the cells in an Ar glovebox and extracting the NMC811 electrodes. Two or three cells were cycled to each potential. Each electrode was carefully washed with 150  $\mu$ L of ethyl methyl carbonate (Sigma-Aldrich, 99%). SEM images were taken of at least three places on each electrode, and approximately 80–100 particles were visible in each image. A particle fracture ratio was calculated by counting the number of fractured particles divided by the total number of particles in the image. Only particles with a minimum visible dimension of 10  $\mu$ m were counted to prevent overcounting particle fragments and unclear particles. The analysis was performed manually in a single-blind manner by multiple people, in which the researchers were unaware of the battery and potential to which the electrode in each image had been subjected. The particle fracture ratio was averaged across the images, and batteries were cycled to each potential (at least six separate images with at least 600 total particles counted per potential). A particle fracture rate was determined by calculating the rate of change between the averaged particle fracture ratios at adjacent potentials by using the scan rate of the cyclic voltammogram. Additional details and raw data can be found in the Section S4.

## RESOURCE AVAILABILITY

### Lead contact

Further information and requests for resources and reagents should be directed to and will be fulfilled by the lead contact, Martin Z. Bazant ([bazant@mit.edu](mailto:bazant@mit.edu)).

### Materials availability

This study did not generate any new or unique materials.

### Data and code availability

The acoustic emissions and electrochemical data and analysis code used in this work are available on Zenodo at <https://doi.org/10.5281/zenodo.16749543> as of the date of publication.

## ACKNOWLEDGMENTS

This work was supported by the Toyota Research Institute through D3BATT: Center for Data-Driven-Design of Li-Ion Batteries. Additional support was provided by the Center for Battery Sustainability. Y.S. acknowledges support from the National Science Foundation Graduate Research Fellowship under grant no. 2141064. A.E.C. acknowledges support from the Department of Defense (DoD) through the National Defense Science and Engineering Graduate (NDSEG) Fellowship Program. SEM imaging was performed in the MIT.nano Characterization Facilities at MIT. The authors would also like to acknowledge Debbie Zhuang, Shakul Pathak, Michael L. Li, Leah S. Soldner, and Young Ko for valuable discussions.

## AUTHOR CONTRIBUTIONS

Conceptualization, Y.S., D.A.C., and M.Z.B.; methodology, Y.S. and D.A.C.; investigation, Y.S., D.A.C., and A.E.C.; formal analysis, Y.S., D.A.C., and A.E.C.; writing – original draft, Y.S.; writing – review and editing, Y.S., D.A.C., A.E.C., and M.Z.B.; supervision, M.Z.B.

## DECLARATION OF INTERESTS

The authors declare no competing interests.

## DECLARATION OF GENERATIVE AI AND AI-ASSISTED TECHNOLOGIES

During the preparation of this work, the author(s) did not use any generative AI or AI-assisted technologies.

## SUPPLEMENTAL INFORMATION

Supplemental information can be found online at <https://doi.org/10.1016/j.joule.2025.102108>.

Received: February 7, 2025

Revised: May 1, 2025

Accepted: August 11, 2025

## REFERENCES

- Goodenough, J.B., and Park, K.-S. (2013). The Li-Ion Rechargeable Battery: A Perspective. *J. Am. Chem. Soc.* **135**, 1167–1176. <https://doi.org/10.1021/ja3091438>.
- Kabir, M.M., and Demirocak, D.E. (2017). Degradation mechanisms in Li-ion batteries: a state-of-the-art review: Degradation Mechanisms in Li-ion Batteries: A State-of-the-Art Review. *Int. J. Energy Res.* **41**, 1963–1986. <https://doi.org/10.1002/er.3762>.
- Birk, C.R., Roberts, M.R., McTurk, E., Bruce, P.G., and Howey, D.A. (2017). Degradation diagnostics for lithium ion cells. *J. Power Sources* **341**, 373–386. <https://doi.org/10.1016/j.jpowsour.2016.12.011>.
- Berecibar, M., Gandiaga, I., Villarreal, I., Omar, N., Van Mierlo, J., and Van Den Bossche, P. (2016). Critical review of state of health estimation methods of Li-ion batteries for real applications. *Renew. Sustain. Energy Rev.* **56**, 572–587. <https://doi.org/10.1016/j.rser.2015.11.042>.
- Osaka, T., Mukoyama, D., and Nara, H. (2015). Review—Development of Diagnostic Process for Commercially Available Batteries, Especially Lithium Ion Battery, by Electrochemical Impedance Spectroscopy. *J. Electrochem. Soc.* **162**, A2529–A2537. <https://doi.org/10.1149/2.0141514jes>.
- Zhuang, D., Li, M.L., Lam, V.N., Braatz, R.D., Chueh, W.C., and Bazant, M.Z. (2024). Physics-Informed Design of Hybrid Pulse Power Characterization Tests for Rechargeable Batteries. *J. Electrochem. Soc.* **171**, 050510. <https://doi.org/10.1149/1945-7111/ad4394>.
- Rhyu, J., Zhuang, D., Bazant, M.Z., and Braatz, R.D. (2024). Optimum Model-Based Design of Diagnostics Experiments (DOE) with Hybrid Pulse Power Characterization (HPPC) for Lithium-Ion Batteries. *J. Electrochem. Soc.* **171**, 070544. <https://doi.org/10.1149/1945-7111/ad63ce>.
- Wang, Z., Li, Z., and Liu, Q. (2011). Infrared thermography non-destructive evaluation of lithium-ion battery. *Proc. Soc. Photo Opt. Instrum. Eng.* <https://doi.org/10.1117/12.901592>.
- Yufit, V., Shearing, P., Hamilton, R.W., Lee, P.D., Wu, M., and Brandon, N.P. (2011). Investigation of lithium-ion polymer battery cell failure using X-ray computed tomography. *Electrochim. Commun.* **13**, 608–610. <https://doi.org/10.1016/j.elecom.2011.03.022>.
- Butler, L.G., Schillinger, B., Ham, K., Dobbins, T.A., Liu, P., and Vajo, J.J. (2011). Neutron imaging of a commercial Li-ion battery during discharge: Application of monochromatic imaging and polychromatic dynamic tomography. *Nucl. Instrum. Methods Phys. Res. Sect. A* **651**, 320–328. <https://doi.org/10.1016/j.nima.2011.03.023>.
- Chacón, X.C.A., Laureti, S., Ricci, M., and Cappuccino, G. (2023). A Review of Non-Destructive Techniques for Lithium-Ion Battery Performance Analysis. *WEVJ* **14**, 305. <https://doi.org/10.3390/wevj14110305>.
- Scrub, C.B. (1987). An introduction to acoustic emission. *J. Phys. E* **20**, 946–953. <https://doi.org/10.1088/0022-3735/20/8/001>.
- L.E. Kinsler, ed. (2000). *Fundamentals of Acoustics, Fourth Edition* (John Wiley & Sons).
- Boyd, W.R., and Varley, J. (2001). The uses of passive measurement of acoustic emissions from chemical engineering processes. *Chem. Eng. Sci.* **56**, 1749–1767. [https://doi.org/10.1016/S0009-2509\(00\)00540-6](https://doi.org/10.1016/S0009-2509(00)00540-6).
- Hsieh, A.G., Bhadra, S., Hertzberg, B.J., Gjeltema, P.J., Goy, A., Fleischer, J.W., and Steingart, D.A. (2015). Electrochemical-acoustic time of flight: in operando correlation of physical dynamics with battery charge and health. *Energy Environ. Sci.* **8**, 1569–1577. <https://doi.org/10.1039/C5EE00111K>.
- Bommier, C., Chang, W., Lu, Y., Yeung, J., Davies, G., Mohr, R., Williams, M., and Steingart, D. (2020). In Operando Acoustic Detection of Lithium Metal Plating in Commercial LiCoO<sub>2</sub>/Graphite Pouch Cells. *Cell Rep. Phys. Sci.* **1**, 100035. <https://doi.org/10.1016/j.xrpp.2020.100035>.
- Pham, M.T.M., Darst, J.J., Finegan, D.P., Robinson, J.B., Heenan, T.M.M., Kok, M.D.R., Iacoviello, F., Owen, R., Walker, W.Q., Magdysyuk, O.V., et al. (2020). Correlative acoustic time-of-flight spectroscopy and X-ray imaging to investigate gas-induced delamination in lithium-ion pouch cells during thermal runaway. *J. Power Sources* **470**, 228039. <https://doi.org/10.1016/j.jpowsour.2020.228039>.
- Chang, W., Mohr, R., Kim, A., Raj, A., Davies, G., Denner, K., Park, J.H., and Steingart, D. (2020). Measuring effective stiffness of Li-ion batteries via acoustic signal processing. *J. Mater. Chem. A* **8**, 16624–16635. <https://doi.org/10.1039/DOTA05552B>.
- Komagata, S., Kuwata, N., Baskaran, R., Kawamura, J., Sato, K., and Mizusaki, J. (2010). Detection of Degradation of Lithium-Ion Batteries with

- Acoustic Emission Technique. *ECS Trans.* 25, 163–167. <https://doi.org/10.1149/1.3334804>.
20. Zhang, K., Yin, J., and He, Y. (2021). Acoustic Emission Detection and Analysis Method for Health Status of Lithium Ion Batteries. *Sensors (Basel)* 21, 712. <https://doi.org/10.3390/s21030712>.
21. Fordham, A., Joo, S.-B., Owen, R.E., Galionas, E., Buckwell, M., Brett, D. J.L., Shearing, P.R., Jervis, R., and Robinson, J.B. (2024). Investigating the Performance and Safety of Li-Ion Cylindrical Cells Using Acoustic Emission and Machine Learning Analysis. *J. Electrochem. Soc.* 171, 070521. <https://doi.org/10.1149/1945-7111/ad59c9>.
22. Beganovic, N., and Söffker, D. (2019). Estimation of Remaining Useful Lifetime of Lithium-Ion Battery Based on Acoustic Emission Measurements. *J. Energy Resour. Technol.* 141, 041901. <https://doi.org/10.1115/1.4042234>.
23. Zhang, K., Tang, L., Fan, W., He, Y., and Rao, J. (2024). Aging and Echelon Utilization Status Monitoring of Power Batteries Based on Improved EMD and PCA of Acoustic Emission. *IEEE Sens. J.* 24, 12142–12152. <https://doi.org/10.1109/JSEN.2024.3370739>.
24. Ohzuku, T., Tomura, H., and Sawai, K. (1997). Monitoring of Particle Fracture by Acoustic Emission during Charge and Discharge of Li / MnO<sub>2</sub> Cells. *J. Electrochem. Soc.* 144, 3496–3500. <https://doi.org/10.1149/1.1838039>.
25. Sawai, K., Tomura, H., and Ohzuku, T. (1998). Acoustic Emission Histometry for Battery Material Research. *Denki Kagaku Oyobi Kogyo Butsuri Kagaku* 66, 301–307. <https://doi.org/10.5796/kogyobutsurikagaku.66.301>.
26. Didier-Laurent, S., Idrissi, H., and Roué, L. (2008). In-situ study of the cracking of metal hydride electrodes by acoustic emission technique. *J. Power Sources* 179, 412–416. <https://doi.org/10.1016/j.jpowsour.2007.12.073>.
27. Kircheva, N., Genies, S., Brun-Buisson, D., and Thivel, P.-X. (2011). Study of Solid Electrolyte Interface Formation and Lithium Intercalation in Li-Ion Batteries by Acoustic Emission. *J. Electrochem. Soc.* 159, A18–A25. <https://doi.org/10.1149/2.045201jes>.
28. Rhodes, K., Dudney, N., Lara-Curcio, E., and Daniel, C. (2010). Understanding the Degradation of Silicon Electrodes for Lithium-Ion Batteries Using Acoustic Emission. *J. Electrochem. Soc.* 157, A1354. <https://doi.org/10.1149/1.3489374>.
29. Kalnajs, S., Rhodes, K., and Daniel, C. (2011). A study of lithium ion intercalation induced fracture of silicon particles used as anode material in Li-ion battery. *J. Power Sources* 196, 8116–8124. <https://doi.org/10.1016/j.jpowsour.2011.05.049>.
30. Tranchot, A., Etiemble, A., Thivel, P.-X., Idrissi, H., and Roué, L. (2015). In-situ acoustic emission study of Si-based electrodes for Li-ion batteries. *J. Power Sources* 279, 259–266. <https://doi.org/10.1016/j.jpowsour.2014.12.126>.
31. Schieles, A., Breitung, B., Mazilkin, A., Schweidler, S., Janek, J., Gumbel, S., Fleischmann, S., Burakowska-Meise, E., Sommer, H., and Brezesinski, T. (2018). Silicon Nanoparticles with a Polymer-Derived Carbon Shell for Improved Lithium-Ion Batteries: Investigation into Volume Expansion, Gas Evolution, and Particle Fracture. *ACS Omega* 3, 16706–16713. <https://doi.org/10.1021/acsomega.8b02541>.
32. Schweidler, S., Bianchini, M., Hartmann, P., Brezesinski, T., and Janek, J. (2020). The Sound of Batteries: An Operando Acoustic Emission Study of the LiNiO<sub>2</sub> Cathode in Li-Ion Cells. *Batteries Supercaps* 3, 1021–1027. <https://doi.org/10.1002/batt.202000099>.
33. Woodford, W.H., Carter, W.C., and Chiang, Y.-M. (2012). Design criteria for electrochemical shock resistant battery electrodes. *Energy Environ. Sci.* 5, 8014. <https://doi.org/10.1039/c2ee21874g>.
34. Choe, C.-Y., Jung, W.S., Jung, W.-S., Byeon, J.-W., and Byeon, J.-W. (2015). Damage Evaluation in Lithium Cobalt Oxide/Carbon Electrodes of Secondary Battery by Acoustic Emission Monitoring. *Mater. Trans.* 56, 269–273. <https://doi.org/10.2320/matertrans.M2014396>.
35. Villevieille, C., Boinet, M., and Monconduit, L. (2010). Direct evidence of morphological changes in conversion type electrodes in Li-ion battery by acoustic emission. *Electrochem. Commun.* 12, 1336–1339. <https://doi.org/10.1016/j.elecom.2010.07.014>.
36. Lemarié, Q., Alloin, F., Thivel, P.X., Idrissi, H., and Roué, L. (2019). Study of sulfur-based electrodes by operando acoustic emission. *Electrochim. Acta* 299, 415–422. <https://doi.org/10.1016/j.electacta.2019.01.019>.
37. Espinoza Ramos, I., Coric, A., Su, B., Zhao, Q., Eriksson, L., Krysander, M., Ahlberg Tidblad, A., and Zhang, L. (2024). Online acoustic emission sensing of rechargeable batteries: technology, status, and prospects. *J. Mater. Chem. A* 12, 23280–23296. <https://doi.org/10.1039/D4TA04571H>.
38. Huguet, S., Godin, N., Gaertner, R., Salmon, L., and Villard, D. (2002). Use of acoustic emission to identify damage modes in glass fibre reinforced polyester. *Compos. Sci. Technol.* 62, 1433–1444. [https://doi.org/10.1016/S0266-3538\(02\)00087-8](https://doi.org/10.1016/S0266-3538(02)00087-8).
39. Anastassopoulos, A., and Philippidis, T. (1997). Clustering methodology for the evaluation of acoustic emission from composites. *NDT E Int.* 30, 108. [https://doi.org/10.1016/S0963-8695\(97\)85511-9](https://doi.org/10.1016/S0963-8695(97)85511-9).
40. Vi-Tong, E., and Gaillard, P. (1987). An algorithm for non-supervised sequential classification of signals. *Pattern Recognit. Lett.* 5, 307–313. [https://doi.org/10.1016/0167-8655\(87\)90071-7](https://doi.org/10.1016/0167-8655(87)90071-7).
41. Schweidler, S., Dreyer, S.L., Breitung, B., and Brezesinski, T. (2021). Operando acoustic emission monitoring of degradation processes in lithium-ion batteries with a high-entropy oxide anode. *Sci. Rep.* 11, 23381. <https://doi.org/10.1038/s41598-021-02685-2>.
42. Schweidler, S., Dreyer, S.L., Breitung, B., and Brezesinski, T. (2022). Acoustic Emission Monitoring of High-Entropy Oxyfluoride Rock-Salt Cathodes during Battery Operation. *Coatings* 12, 402. <https://doi.org/10.3390/coatings12030402>.
43. Etiemble, A., Idrissi, H., Meille, S., and Roué, L. (2012). In situ investigation of the volume change and pulverization of hydride materials for Ni-MH batteries by concomitant generated force and acoustic emission measurements. *J. Power Sources* 205, 500–505. <https://doi.org/10.1016/j.jpowsour.2012.01.066>.
44. An, S.J., Li, J., Daniel, C., Mohanty, D., Nagpure, S., and Wood, D.L. (2016). The state of understanding of the lithium-ion-battery graphite solid electrolyte interphase (SEI) and its relationship to formation cycling. *Carbon* 105, 52–76. <https://doi.org/10.1016/j.carbon.2016.04.008>.
45. Parks, H.C.W., Boyce, A.M., Wade, A., Heenan, T.M.M., Tan, C., Martínez-Pañeda, E., Shearing, P.R., Brett, D.J.L., and Jervis, R. (2023). Direct observations of electrochemically induced intergranular cracking in polycrystalline NMC811 particles. *J. Mater. Chem. A* 11, 21322–21332. <https://doi.org/10.1039/D3TA03057A>.
46. Bard, A.J., and Faulkner, L.R. (2001). *Electrochemical Methods: Fundamentals and Applications*. edition2 (John Wiley & Sons).
47. Heyrovsky, J. (1960). Trends in Polarography. *Science* 132, 123–130. <https://doi.org/10.1126/science.132.3420.123>.
48. Bacmaga, J., Stimac, H., Gillon, R., and Baric, A. (2020). High-Frequency Characterization and Parametrized Modeling of DC-Biased Surface-Mount Ferrite Beads for EMI Suppression Applications. *IEEE Trans. Electromagn. Compat.* 62, 2793–2803. <https://doi.org/10.1109/TEMC.2020.2996310>.
49. Li, J., Downie, L.E., Ma, L., Qiu, W., and Dahn, J.R. (2015). Study of the Failure Mechanisms of LiNi<sub>0.8</sub>Mn<sub>0.1</sub>Co<sub>0.1</sub>O<sub>2</sub> Cathode Material for Lithium Ion Batteries. *J. Electrochem. Soc.* 162, A1401–A1408. <https://doi.org/10.1149/2.1011507jes>.
50. Sun, H.-H., and Manthiram, A. (2017). Impact of Microcrack Generation and Surface Degradation on a Nickel-Rich Layered Li[Ni<sub>0.9</sub>Co<sub>0.05</sub>Mn<sub>0.05</sub>]O<sub>2</sub> Cathode for Lithium-Ion Batteries. *Chem. Mater.* 29, 8486–8493. <https://doi.org/10.1021/acs.chemmater.7b03268>.
51. Llanos, P.S., Ahaliabadeh, Z., Miikkulainen, V., Lahtinen, J., Yao, L., Jiang, H., Kankaanpää, T., and Kallio, T.M. (2024). High Voltage Cycling Stability of LiF-Coated NMC811 Electrode. *ACS Appl. Mater. Interfaces* 16, 2216–2230. <https://doi.org/10.1021/acsami.3c14394>.

52. Wade, A., Llewellyn, A.V., Heenan, T.M.M., Tan, C., Brett, D.J.L., Jervis, R., and Shearing, P.R. (2023). First Cycle Cracking Behaviour Within Ni-Rich Cathodes During High-Voltage Charging. *J. Electrochem. Soc.* 170, 070513. <https://doi.org/10.1149/1945-7111/ace130>.
53. Parks, H.C.W., Jones, M.P., Wade, A., Llewellyn, A.V., Tan, C., Reid, H.T., Ziesche, R., Heenan, T.M.M., Marathe, S., Rau, C., et al. (2025). Non-linear cracking response to voltage revealed by operando X-ray tomography in polycrystalline NMC811. *EES Batteries* 1, 482–494. <https://doi.org/10.1039/D5EB00008D>.
54. Smith, A., and Dixon, N. (2019). Acoustic emission behaviour of dense sands. *Géotechnique* 69, 1107–1122. <https://doi.org/10.1680/jgeot.18.P.209>.
55. Ipers, G., Jiao, J., Pathak, S., Fang, R., Berliner, M.D., Li, W., Li, W., Braatz, R.D., Bazant, M.Z., and Zhu, J. (2024). Rapid Simulation of Electro-Chemo-Mechanical Deformation of Li-ion Batteries Based On Porous Electrode Theory. *J. Electrochem. Soc.* 171, 050557. <https://doi.org/10.1149/1945-7111/ad4f1e>.
56. Zhu, J., Li, W., Wierzbicki, T., Xia, Y., and Harding, J. (2019). Deformation and failure of lithium-ion batteries treated as a discrete layered structure. *Int. J. Plast.* 121, 293–311. <https://doi.org/10.1016/j.ijplas.2019.06.011>.
57. Drucker, D.C., and Prager, W. (1952). Soil mechanics and plastic analysis or limit design. *Quart. Appl. Math.* 10, 157–165. <https://doi.org/10.1090/qam/48291>.
58. Deshpande, V.S., and Fleck, N.A. (2000). Isotropic constitutive models for metallic foams. *J. Mech. Phys. Solids* 48, 1253–1283. [https://doi.org/10.1016/S0022-5096\(99\)00082-4](https://doi.org/10.1016/S0022-5096(99)00082-4).
59. Gu, C., Kim, M., and Anand, L. (2001). Constitutive equations for metal powders: application to powder forming processes. *Int. J. Plast.* 17, 147–209. [https://doi.org/10.1016/S0749-6419\(00\)00029-2](https://doi.org/10.1016/S0749-6419(00)00029-2).
60. Ryu, H.-H., Lee, S.-B., Yoon, C.S., and Sun, Y.-K. (2022). Morphology-Dependent Battery Performance of Ni-Rich Layered Cathodes: Single-Crystal versus Refined Polycrystal. *ACS Energy Lett.* 7, 3072–3079. <https://doi.org/10.1021/acsenergylett.2c01670>.
61. Li, J., Cameron, A.R., Li, H., Glazier, S., Xiong, D., Chatzidakis, M., Allen, J., Botton, G.A., and Dahn, J.R. (2017). Comparison of Single Crystal and Polycrystalline  $\text{LiNi}_{0.5}\text{Mn}_{0.3}\text{Co}_{0.2}\text{O}_2$  Positive Electrode Materials for High Voltage Li-Ion Cells. *J. Electrochem. Soc.* 164, A1534–A1544. <https://doi.org/10.1149/2.0991707jes>.
62. Weber, R., Fell, C.R., Dahn, J.R., and Hy, S. (2017). Operando X-ray Diffraction Study of Polycrystalline and Single-Crystal  $\text{Li}_{x}\text{Ni}_{0.5}\text{Mn}_{0.3}\text{Co}_{0.2}\text{O}_2$ . *J. Electrochem. Soc.* 164, A2992–A2999. <https://doi.org/10.1149/2.0441713jes>.
63. Oswald, S., Pritzl, D., Wetjen, M., and Gasteiger, H.A. (2020). Novel Method for Monitoring the Electrochemical Capacitance by In Situ Impedance Spectroscopy as Indicator for Particle Cracking of Nickel-Rich NCMs: Part I. Theory and Validation. *J. Electrochem. Soc.* 167, 100511. <https://doi.org/10.1149/1945-7111/ab9187>.
64. Zhang, B., Metzger, M., Solchenbach, S., Payne, M., Meini, S., Gasteiger, H.A., Garsuch, A., and Lucht, B.L. (2015). Role of 1,3-Propane Sultone and Vinylene Carbonate in Solid Electrolyte Interface Formation and Gas Generation. *J. Phys. Chem. C* 119, 11337–11348. <https://doi.org/10.1021/acs.jpcc.5b00072>.
65. Lin, N., Jia, Z., Wang, Z., Zhao, H., Ai, G., Song, X., Bai, Y., Battaglia, V., Sun, C., Qiao, J., et al. (2017). Understanding the crack formation of graphite particles in cycled commercial lithium-ion batteries by focused ion beam - scanning electron microscopy. *J. Power Sources* 365, 235–239. <https://doi.org/10.1016/j.jpowsour.2017.08.045>.
66. Zhang, W.-J. (2011). Structure and performance of LiFePO<sub>4</sub> cathode materials: A review. *J. Power Sources* 196, 2962–2970. <https://doi.org/10.1016/j.jpowsour.2010.11.113>.
67. Märker, K., Reeves, P.J., Xu, C., Griffith, K.J., and Grey, C.P. (2019). Evolution of Structure and Lithium Dynamics in LiNi<sub>0.8</sub>Mn<sub>0.1</sub>Co<sub>0.1</sub>O<sub>2</sub> (NMC811) Cathodes during Electrochemical CyclingLiNiO. *Chem. Mater.* 31, 2545–2554. <https://doi.org/10.1021/acs.chemmater.9b00140>.
68. Matsuo, T., Uchida, M., and Cho, H. (2011). Development of Acoustic Emission Clustering Method to Detect Degradation of Lithium Ion Batteries. *JMMP* 5, 678–689. <https://doi.org/10.1299/jmmp.5.678>.
69. Takahashi, K., and Srinivasan, V. (2015). Examination of Graphite Particle Cracking as a Failure Mode in Lithium-Ion Batteries: A Model-Experimental Study. *J. Electrochem. Soc.* 162, A635–A645. <https://doi.org/10.1149/2.0281504jes>.
70. Jung, R., Metzger, M., Maglia, F., Stinner, C., and Gasteiger, H.A. (2017). Oxygen Release and Its Effect on the Cycling Stability of  $\text{LiNi}_x\text{Mn}_y\text{Co}_z\text{O}_2$  (NMC) Cathode Materials for Li-Ion Batteries. *J. Electrochem. Soc.* 164, A1361–A1377. <https://doi.org/10.1149/2.0021707jes>.
71. Jung, R., Metzger, M., Maglia, F., Stinner, C., and Gasteiger, H.A. (2017). Chemical versus Electrochemical Oxidation on NMC111, NMC622, NMC811, LNMO, and Conductive Carbon. *J. Phys. Chem. Lett.* 8, 4820–4825. <https://doi.org/10.1021/acs.jpclett.7b01927>.
72. Burrus, C.S., Gopinath, R.A., and Guo, H. (1998). *Introduction to Wavelets and Wavelet Transforms: a Primer* (Prentice Hall).
73. Debnath, L., and Shah, F.A. (2015). *Wavelet Transforms and Their Applications*, Second Edition (Birkhäuser Verlag). <https://doi.org/10.1007/978-0-8176-8418-1>.
74. Lin, J., and Qu, L. (2000). Feature Extraction based on Morlet Wavelet and its Application for Mechanical Fault Diagnosis. *J. Sound Vib.* 234, 135–148. <https://doi.org/10.1006/jsvi.2000.2864>.
75. Torgerson, W.S. (1952). Multidimensional Scaling: I. Theory and Method. *Psychometrika* 17, 401–419. <https://doi.org/10.1007/BF02288916>.